Received: 21 April 2023 | Revised: 23 May 2023 | Accepted: 3 June 2023

DOI: 10.1111/ijac.14476

Applied Ceramic TECHNOLOGY

RESEARCH ARTICLE

# Structural and thermodynamic analysis of metal filler incorporations in $Si_aO_b(M)_cC_d$ polymer derived ceramics: Ta, Hf, Nb

**Gerson J. Leonel**[1,2] | **Manuel Scharrer**[1,2] | **Gurpreet Singh**[3] | **Alexandra Navrotsky**[1,2]

[1]School of Molecular Sciences and Center for Materials of the Universe, Arizona State University, Tempe, Arizona, USA

[2]Navrotsky Eyring Center for Materials of the Universe, School of Molecular Sciences, Arizona State University, Tempe, Arizona, USA

[3]Mechanical and Nuclear Engineering Department, Kansas State University, Manhattan, Kansas, USA

**Correspondence**
Alexandra Navrotsky, School of Molecular Sciences and Center for Materials of the Universe, Arizona State University, Tempe, AZ 85287, USA.
Email: Alexandra.navrotsky@asu.edu

**Funding information**
National Science Foundation (NSF) Partnerships for International Research and Education (PIRE), Grant/Award Number: #1743701

**Abstract**

This work systematically investigates the thermodynamic stability of $Si_aO_b(M)_cC_d$ structures derived from polymeric precursors incorporating metal fillers: Ta, Nb, and Hf, at 1200 and 1500°C. Structural characterization of the polymer derived ceramics (PDCs) employs X-ray diffraction, Fourier transform infrared spectroscopy, and X-ray photoelectron spectroscopy. Enthalpies of formation relative to crystalline components (metal oxide, silica, silicon carbide, and graphite) are obtained from thermodynamic measurements by high temperature oxide melt solution calorimetry. The enthalpies of formation ($\Delta H°_{f,\,comp}$) of Ta-1200, Hf-1200, Nb-1200, Ta-1500, Hf-1500, and Nb-1500 specimens are −137.82 ± 9.72, −256.31 ± 8.97, −82.80 ± 9.82, −182.80 ± 7.85, −292.54 ± 9.38, −224.98 ± 9.60 kJ/mol, respectively. Overall incorporation of Hf results in most thermodynamically stable structures at all synthesis temperatures. $Si_aO_b(M)_cC_d$ specimens employing Nb fillers undergo the most stable structural evolution in this temperature range. The results indicate strong thermodynamic drive for carbothermal reduction of metal oxide domains. Incorporation of Ta provides the greatest stabilization of $SiO_3C$ mixed bonding environments. Ultimately, the choice of metal filler influences composition, structural evolution, and thermodynamic stability in PDCs.

**KEYWORDS**
phase equilibria, silicon oxycarbide, thermodynamics

## 1 | INTRODUCTION

The processing of organometallic precursors such as polysilazanes, polycarbosilanes, and polysiloxanes at elevated temperatures permits attainability of $Si_xC_yN_z$, $Si_xC_y$, and $Si_xO_yC_z$ refractory materials with high chemical, thermal, and mechanical stability.[1,2] Over the past five decades the synthesis of carbide, nitride, and oxide ceramic materials through the polymeric route has increased in popularity.[1] Polymer derived ceramics (PDCs) are especially attractive due to spinnability of the precursors, which permits attainability of ceramic fibers.[3–5] Additionally, appropriate processing of preceramic polymers permits development of high temperature ceramic films.[6,7] This is especially important in response to current interest for the development

  

of protective coatings for application in aerospace systems.[8–11]

Tunability of preceramic polymer viscosity is possible by use of appropriate additives and this enables moldability of the precursor, which can then be pyrolyzed into near net shape ceramic materials, without the need for further processing.[12–16] This is important in additive manufacturing, since it eliminates the need for subsequent shaping of sintered ceramics during manufacturing of ceramic components (valves, bearings, seals).[13] Beyond dimensional tunability, the PDC route permits modulation of the microstructure in nominally similar ceramics through manipulation of chemical groups in the oligomers.[1] This matters because in PDCs minor microstructural differences can result in significant dissimilarities in their physicochemical properties (e.g., *persistence to thermal degradation*).[2,17]

PDCs like SiOCs have complex microstructures, typically comprised of X-ray -amorphous free carbon (C), silica ($SiO_2$), silicon carbide (SiC), and mixed bonding domains.[2] In mixed bonding networks silicon (Si) is bonded to both oxygen (O) and carbon (C).[18–20] The complex nature of PDC structures makes precise structural characterization challenging. Ceramics synthesized at lower temperatures (~1200°C) tend to be amorphous, however higher synthesis temperatures (>1450°C), which are most used in ceramic matrix composite processing, can result in crystallization of silicon carbide (SiC) domains.[21–23]

Recent PDC works highlight incorporation of fillers (sacrificial, active, passive) in ceramic structures.[24,25] The use of sacrificial fillers like polymethylmethacrylate typically results in increased porosity of the final ceramics.[26] Similarly, active metallic or intermetallic fillers can reduce volume shrinkage of preceramic polymers during thermal treatment.[1] Other studies have also demonstrated greater resistance to crystallization in PDCs incorporating boron.[27] As the use of PDC fillers increases, it is essential to understand how choice of filler influences composition as well as microstructure.[28–32] It is especially important to identify the effect of filler and corresponding structural modification on the thermodynamic stability of the respective ceramics, since stability determines propensity for phase separation and decomposition in PDCs.[5,33–37]

In the past, thermodynamic works investigated structure-stability relations in various PDC systems, including the effect of composition, mixed bonding, and pyrolysis temperature on the thermodynamic stability.[5,34,37] To this end, the present paper is the first work to systematically investigate the structural evolution and thermodynamic stabilization in PDCs incorporating Hf, Nb, and Ta. We report the synthesis,

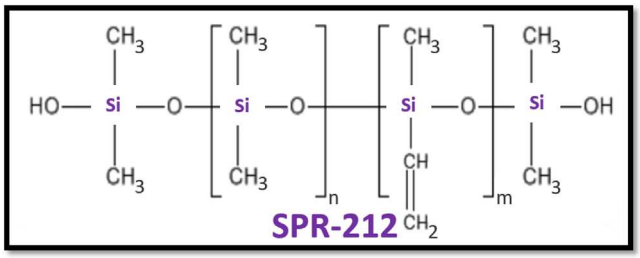


**FIGURE 1** Structure of single source industrial precursor (SPR-212) for SiOCs.

characterization, and thermodynamic analysis of the structures synthesized at 1200 and 1500°C. Structural and chemical characterization are done by X-ray diffraction (XRD), Fourier transform infrared spectroscopy (FTIR), and X-ray photoelectron spectroscopy (XPS). Thermodynamic measurements employ high temperature oxide melt solution calorimetry. This work permits assessment of the influence of choice of metal filler as well as of synthesis temperature on the composition, structure, and thermodynamic stability of SiO(M)Cs (where M = metal), thus permitting identification of the energy landscape for metal filler incorporation in PDCs.

## 2 | EXPERIMENTAL METHODS

### 2.1 | Materials and crosslinking

The liquid siloxane SPR-2012 (stored in a laboratory freezer) from Starfire Systems was used as polymeric precursor for the PDCs. Structure of the precursor is shown in Figure 1. The preceramic polymer (equilibrated to ambient temperature for ~12 h) is mixed with 30 wt % of either Hf, Nb, or Ta metal powders (from Fisher Scientific), under magnetic stirring for 1 h in a glovebox employing a nitrogen atmosphere (~.1 ppm oxygen content). This results in Hf, Nb, and Ta modified SPR-212 precursors. Crosslinking of the precursor mixtures is done in a beaker on a hotplate, under inert atmosphere (in glovebox). The hotplate employs a temperature ramping of ~5°C/min. Before pyrolysis, the precursor mixtures are each crosslinked into rigid solids at 300°C ($T_{max}$ of hotplate) for 3 h. It should be noted that during crosslinking (under stirring) significant metal content settles on the bottom and sticks to the walls of the beaker. Localized aggregation of metal powders can be observed throughout the precursors, and this results in metal distribution inhomogeneity across the final crosslinked specimens. We do not employ the use of any crosslinking catalysts in the synthesis of the specimens.

## 2.2 | Pyrolysis

High temperature pyrolysis of the crosslinked precursors is done in a Netzsch STA 409 differential scanning calorimeter cell, using alumina crucibles, under flowing argon atmosphere (50 mL/min). Pyrolysis of precursors is investigated at 1200 and 1500°C. The pyrolysis employs a temperature ramping of 2°C/min to final pyrolysis temperature. This results in the formation of Hf-1200, Nb-1200, Ta-1200, Hf-1500, Nb-1500, and Ta-1500 specimens. The resulting ceramics are then ground into fine powders by the use of an agate mortar and pestle, in the glovebox operating at ambient temperature. During milling each specimen was manually ground for at least 10 min to ensure homogenous mixing in each powdered sample.

## 2.3 | Characterization

XRD experiments employ a table-top Bruker D2 powder diffractometer (nickel-filtered CuK$\alpha$ radiation, wavelength = 1.5418 Å). FTIR employs a Bruker TENSOR instrument with platinum ATR accessory. XPS experiments are done using a Kratos AXIS Supra+, employing monochromatic Al K$\alpha$+ ion beam, with beam energy = 1486.6 eV. For each fine powder, three different locations are selected for XPS experiments.

## 2.4 | Thermochemistry

Calorimetric measurements are done by oxide melt solution calorimetry in a commercial Seteram Alexsys calorimeter. Dissolution of the PDCs occurs in 20 g of sodium molybdate ($3Na_2O{\bullet}MoO_3$) melt, at 800°C. This technique measures enthalpies of dissolution ($\Delta H_{dis}$) and permits quantitation of enthalpies of formation relative to elements ($\Delta H°_{f,\,elem}$) and components ($\Delta H°_{f,\,comp}$). In the first step ~5 mg of the sample is weighed using a Mettler Toledo microbalance (~10 $\mu$g accuracy) and then pressed into a pellet using a 1.5 mm tungsten die. In the second step the pellet is inserted into the calorimeter, where it undergoes oxidative dissolution in the melt. The melt is continuously bubbled with 40 mL/min of oxygen, this ensures continuous oxidative environment. The samples employ oxygen flushing (~100 mL/min) to evacuate any evolved gases resulting from dissolution of the specimen. During dissolution Si is oxidized to cristobalite ($SiO_2$), which precipitates from the melt, C is oxidized to $CO_2$ (evolves from melt), and the metal is oxidized to metal oxide ($Ta_2O_5$, $HfO_2$, $Nb_2O_5$), which dissolves in the melt.[5,37–39] For each sample the experiments are repeated at least six times. More experimental details are provided in previous works.[39]

Reaction (1) describes the oxidative dissolution of $Si_aO_b(M)_cC_d$ specimens, where M = Hf, Nb, or Ta

$$\begin{aligned}&Si_aO_bM_cC_d(s,\ 25°C) + ((2a + 2d + (c/e)\,f) - b)\,/2\,O_2\\&(g,\ 800°C) \rightarrow aSiO_2\,(s,\ 800°C) + d\ CO_2\,(g,\ 800°C)\\&+ (c/e)\,M_eO_f\,(sol,\ 800°C)\,\Delta H^{o}_{dis}\end{aligned} \tag{1}$$

Enthalpy of formation of $Si_aO_b(M)_cC_d$ from the elements (Si, C, M and $O_2$) is described below:

$$\begin{aligned}&aSi\,(s,\ 25°C) + b/2O_2\ \ (g,\ 25°C)\\&+d\,C\,(s,\ 25°C) + c\,M\,(s,\ 25°C) \rightarrow\\&Si_aO_bM_cC_d(s,\ 25°C)\Delta H^{o}_{f,\ elem}\end{aligned} \tag{2}$$

Reactions (3) and (4) describe enthalpy of formation relative to crystalline components ($\beta$-SiC, $SiO_2$ (cristobalite), C (graphite), and most stable metal oxide $M_xO_y$ or carbide $M_xC_y$):

$$\begin{aligned}&(a - ((b - (c/e)\,f)\,/2))\\&SiC\,(s,\ 25°C) + ((b - (c/e)\,f)\,/2)\ SiO_2\,(s,\ 25°C) + (c/e)\\&M_eO_f\,(s,\ 25°C) + (d - (a - ((b - (c/e)\,f)\,/2)))\\&C\,(s,\ 25°C) \rightarrow Si_aO_bM_cC_d(s,\ 25°C)\Delta H^{o}_{f,comp},\\&\text{where } M_eO_f = Ta_2O_5,\ HfO_2,\ \text{or } Nb_2O_5.\end{aligned} \tag{3}$$

$$\begin{aligned}&(a - (b/2))\,SiC\,(s,\ 25°C) + (b/2)\,SiO_2\,(s,\ 25°C)\\&+c\,MC\,(s,\ 25°C) + (d - (a - (b/2)) - c)\,C\,(s,\ 25°C) \rightarrow\\&Si_aO_bM_cC_d(s,\ 25°C)\Delta H^{o}_{f,comp},\\&\text{where } MC = TaC, HfC, \text{or } NbC.\end{aligned} \tag{4}$$

Given that the initial and final states of the system are known, enthalpies of formation are determined by employing enthalpies of dissolution and thermodynamic cycles (Tables 1–4).

# 3 | RESULTS AND DISCUSSION

FTIR permits identification of functional groups in structures. Spectra of the crosslinked precursors and corresponding PDCs are summarized in Figure 2A,B. The intensity of FTIR peaks is proportional to the amount of corresponding bonds.[43,44] The results in Figure 2 indicate

**TABLE 1** Thermochemical cycle for calculation of enthalpy of oxidation $\Delta H^{\circ}_{OX}$, at 25°C.

| **$Si_aO_bM_cC_d$ (s, 25°C) + ((2a + 2d +(c/e)f)-b)/2 $O_2$ (g, 25°C) → a $SiO_2$ (s, 25°C) + d $CO_2$ (g, 25°C) + (c/e) $M_eO_f$ (s, 25°C) $\Delta H^{o}_{dis}$) $\Delta H^{\circ}_{Ox}$ = ?** | **ΔH (kJ/mol)** |
|---|---|
| $Si_aO_bM_cC_d$ (s, 25°C) + ((2a + 2d +(c/e)f)-b)/2 $O_2$ (g, 800°C) → a$SiO_2$ (s, 800°C) + d$CO_2$ (g, 800°C) + (c/e)$M_eO_f$ (sol, 800°C) | $\Delta H_{dis}$ |
| $O_2$ (g, 25°C) → $O_2$ (g, 800°C) | $\Delta H_2 = 25.3$ |
| $SiO_2$ (s, 25 °C) → $SiO_2$ (s, 800 °C) | $\Delta H_3 = 50.1$ |
| $CO_2$ (s, 25°C) → $CO_2$ (g, 800°C) | $\Delta H_4 = 37.5$ |
| $M_eO_f$ (s, 25°C) → $M_eO_f$ (sol, 800°C) | $\Delta H_5 = 108.72 \pm 2$ ($Ta_2O_5$)<br>$= 85.01 \pm 2$ ($HfO_2$)<br>$= 111.50 \pm .16$ ($Nb_2O_5$) |
| $\Delta H^{\circ}_{OX} = \Delta H_{dis} + ((2a + 2d + (c/e)f)\text{-}b)/2\ \Delta H_2 - a\ \Delta H_3 - d\Delta H_4 - (c/e)\ \Delta H_5$ | $\Delta H^{\circ}_{OX}$ |

**TABLE 2** Thermochemical cycle for calculation of enthalpy of formation from elements $\Delta H^{\circ}_{f,\,elem}$, at 25°C.

| **a Si (s, 25°C) + b/2 $O_2$ (g, 25°C + d C (s, 25°C) + c M (g, 25°C)→ $Si_aO_bM_cC_d$ (s, 25°C) $\Delta H^{\circ}_{f,\,elem}$ = ?** | **ΔH (kJ/mol)** |
|---|---|
| $Si_aO_bM_cC_d$ (s, 25°C) + ((a*2+d*2+(c*f/e)-(b))/2) $O_2$ (g, 25°C) → a$SiO_2$ (s, 25°C) + d$CO_2$ (g, 25°C) + (c/e)$M_eO_f$ (s, 25°C) | $\Delta H^{\circ}_{Ox}$ |
| Si (s, 25°C) + $O_2$ (g, 25°C)→$SiO_2$ (s, 25°C) | $\Delta H_2 = -908.4 \pm 2.1$ [40] |
| C (s, 25°C) + $O_2$ (g, 25°C)→$CO_2$ (g, 25°C) | $\Delta H_3 = -393.5 \pm .1$ [40] |
| eM (s, 25°C) + (f/2) $O_2$ (g, 25°C)→$M_eO_f$ (s, 25°C) | $\Delta H_4 = -2045.976$ ($Ta_2O_5$) [40]<br>$= -1899.536$ ($Nb_2O_5$)[40]<br>$= -1117.63 \pm .39$ ($HfO_2$) [41] |
| $\Delta H^{\circ}_{f,\,elem} = -\Delta H_{Ox} + a\ \Delta H_2 + d\ \Delta H_3 + (c/e)\ \Delta H_4$ | $\Delta H^{\circ}_{f,\,elem}$ |

**TABLE 3** Thermochemical cycle for calculation of enthalpy of formation from crystalline components (β-SiC, $SiO_2$ (cristobalite), C (graphite), and metal oxide $M_xO_y$ (metal oxide) $\Delta H^{\circ}_{f,\,comp}$, at 25°C.

| **(a-((b-(c/e)f)/2)) SiC (s, 25°C)+ ((b-(c/e)f)/2) $SiO_2$ (s, 25°C)+ (c/e) $M_eO_f$ (s, 25°C)+ (d-(a-((b-(c/e)f)/2))) C (s, 25°C) → $Si_aO_bM_cC_d$ (s, 25°C) $\Delta H^{o}_{f,comp}$ = ?** | **ΔH (kJ/mol)** |
|---|---|
| aSi (s, 25°C) + b/2$O_2$ (g, 25°C) + dC (s, 25°C) + cM (s, 25°C)→ $Si_aO_bM_cC_d$ (s, 25°C) | $\Delta H^{\circ}_{f,\,elem}$ |
| Si (s, 25°C) + C (s, 25°C)→SiC (s, 25°C) | $\Delta H_2 = -73.2 \pm 6.3$[40] |
| Si (s, 25°C) + $O_2$ (g, 25°C)→$SiO_2$ (s, 25°C) | $\Delta H_3 = -908.4 \pm 2.1$[40] |
| eM (s, 25°C) + (f/2) $O_2$ (g, 25°C)→ $M_eO_f$ (s, 25°C) | $\Delta H_4 = -2045.976$ ($Ta_2O_5$)[40]<br>$= -1899.536$ ($Nb_2O_5$)[40]<br>$= -1117.63 \pm .39$ ($HfO_2$)[41] |
| $\Delta H^{\circ}_{f,\,comp} = \Delta H^{\circ}_{f,\,elem} - (a-((b-(c/e)f)/2))\ \Delta H_2 - ((b\text{-}(c/e)f)/2)\ \Delta H_3 - (c/e)\ \Delta H_4$ | $\Delta H^{\circ}_{f,\,comp}$ |

**TABLE 4** Thermochemical cycle for calculation of enthalpy of formation from crystalline components (β-SiC, $SiO_2$ (cristobalite), C (graphite), and $M_xC_y$ (metal carbide)) $\Delta H^{\circ}_{f,\,comp}$, at 25°C.

| **(a-(b/2)) SiC (s, 25°C)+ (b/2) $SiO_2$ (s, 25°C) + c MC (s, 25°C)+ (d-(a-(b/2))- c) C (s, 25°C) → $Si_aO_bM_cC_d$ (s, 25°C) $\Delta H^{o}_{f,comp}$ = ?** | **ΔH (kJ/mol)** |
|---|---|
| aSi (s, 25°C) + b/2$O_2$ (g, 25°C) + dC (s, 25°C) + cM (s, 25°C)→ $Si_aO_bM_cC_d$ (s, 25°C) | $\Delta H^{\circ}_{f,\,elem}$ |
| Si (s, 25°C) + C (s, 25°C)→SiC (s, 25°C) | $\Delta H_2 = -73.2 \pm 6.3$[40] |
| Si (s, 25°C) + $O_2$ (g, 25°C)→$SiO_2$ (s, 25°C) | $\Delta H_3 = -908.4 \pm 2.1$[40] |
| M (s, 25°C) + C (s, 25°C)→MC (s, 25°C) | $\Delta H_4 = -144.097$ (TaC)[40]<br>$= -138.91$ (NbC)[40]<br>$= -218.82$(HfC)[42] |
| $\Delta H^{\circ}_{f,\,comp} = \Delta H^{\circ}_{f,\,elem} - (a\text{-}(b/2))\ \Delta H_2 - (b/2)\ \Delta H_3 - c\ \Delta H_4$ | $\Delta H^{\circ}_{f,\,comp}$ |

Abbreviations: g, gas; s, solid; sol, solution.

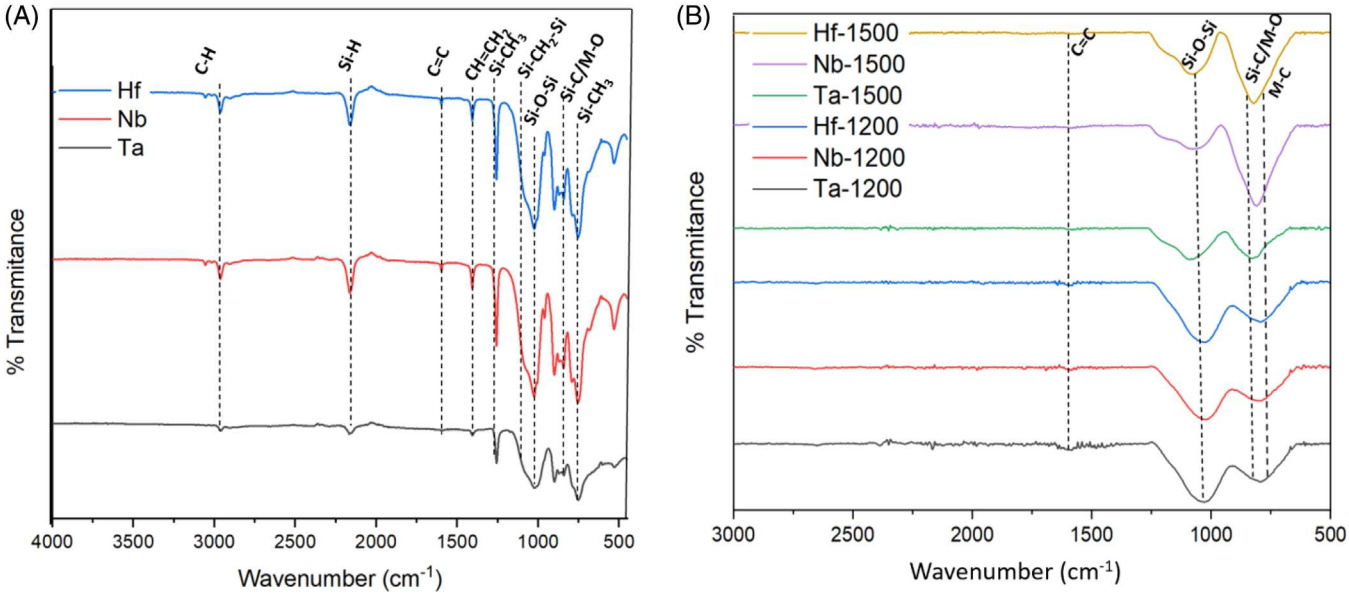


**FIGURE 2** FTIR spectra of (A) crosslinked precursors and (B) corresponding $Si_aO_b(M)_cC_d$ PDCs synthesized at 1200 and 1500°C.

presence of Si–O—Si (~1060 $cm^{-1}$), Si—$CH_3$ (~1260 $cm^{-1}$), C=C (~1600 $cm^{-1}$), Si—O—Si (~1060 $cm^{-1}$), Si—C/M—O (~800 $cm^{-1}$), and M—C (~600 $cm^{-1}$) bond stretch vibrational bands in the specimens.[45–57] The results further point to the evolution of organic groups during high temperature pyrolysis, which is typical during ceramization; thus C-H and Si-H bonds are not observed in the PDCs synthesized at 1200 and 1500°C (see Figure 2). The Si—O—Si and Si—C bonds are consistent with SiOC structures.[48–53]

XRD permits assessment of crystallinity. This allows determination of crystallization behavior in the PDC depending on choice of metal as well as pyrolysis temperature. Typically, SiOCs pyrolyzed below 1250°C are X-ray amorphous, increasing synthesis temperature above 1450°C promotes crystallization of $\beta$-SiC domains.[21–23] All $Si_aO_b(M)_cC_d$ samples display peaks corresponding to some identifiable metal carbide and oxide phases. The results in Figure 3 further indicate crystallization of $\beta$-SiC domains (main peaks at $2\theta = 35.60°$, 60°, and 72°) in PDCs pyrolyzed at 1500°C.[58,59] The unidentified XRD peaks may correspond to other crystalline metal oxide, carbide or oxycarbide phases. Overall, all samples display increase in the relative intensity of peaks corresponding to metal carbide with increasing synthesis temperature. This could imply carbothermal reduction of metal oxide phases at higher synthesis temperature (1500°C).[60–62]

High–Resolution (HR)-XPS identification of bonding environments in PDC microstructures is done by surveying Si 2p, C 1s, O 1s, Ta 4f, Nb 3d, and Hf 4f bonds.[5,33] The results are summarized in Figure 4. By employing suitable curve fitting, the area under the convolution curves is proportional to the relative amount of corresponding

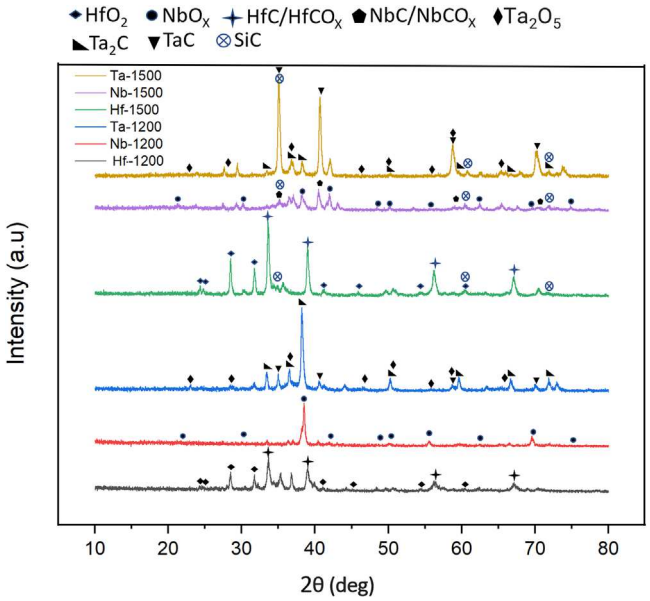


**FIGURE 3** XRD patterns of $Si_aO_b(M)_cC_d$ ceramics. The results show significant crystallization of metal oxide and/or carbide phases in all PDCs.

bonds in the microstructures.[63] This permits semiquantitative assessment of microstructural differences in samples, resulting from choice of metal filler and pyrolysis temperature.

Si 2p convolutions suggest presence of $SiO_4$ (~104 eV), $SiOC_3$ (~101.5 eV), $SiO_2C_2$ (~102 eV) and $SiO_3C$ (~102.9 eV) bonds in all samples.[64,65] Generally, $SiO_4$ bonds correspond to amorphous silica ($SiO_2$) domains. Overall, the relative amount of $SiO_4$ bonds appears to

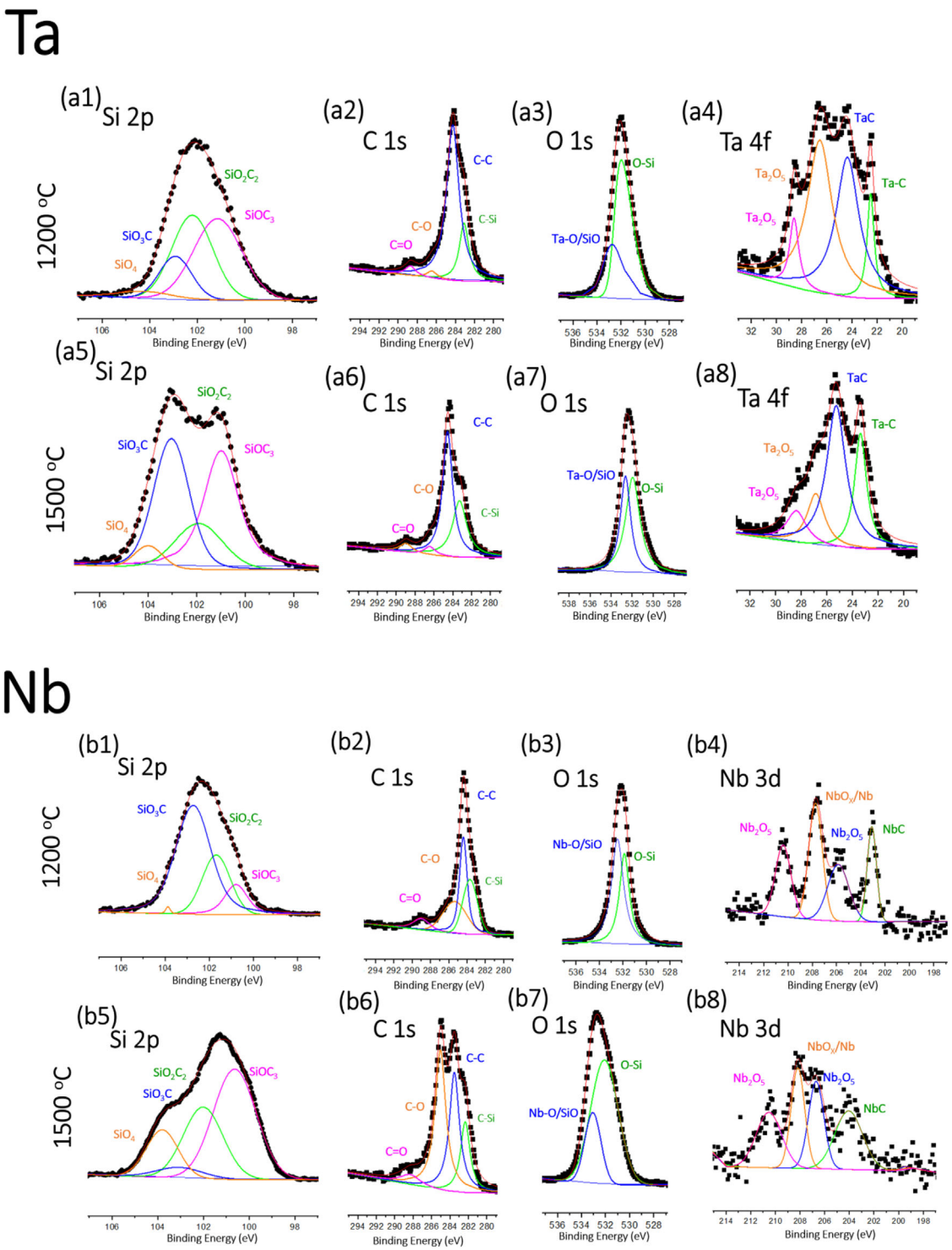


**FIGURE 4** HR–XPS of the PDCs synthesized from metal modified SiOC precursors, under flowing argon atmosphere, at 1200 and 1500°C.

increase with synthesis temperature, which is consistent with phase separation of the amorphous $Si_aO_bC_c$ microstructure at higher temperatures. The results further indicate presence of $SiO_2C_2$, $SiOC_3$, and $SiO_3C$ bonds, and this corresponds to $SiO_xC_{4-x}$ mixed bonding environments (Si bonded to O and C) in the samples, which is typical in PDCs.[19] The results in Figure 4 show general increase of $SiOC_3$ compared to $SiO_3C$ mixed bonds with increasing synthesis temperature, and this may indicate greater resistance to thermal degradation of $SiOC_3$ mixed bonding networks. However, it should be highlighted that addition of Ta may promote thermal stabilization of $SiO_3C$ bonds

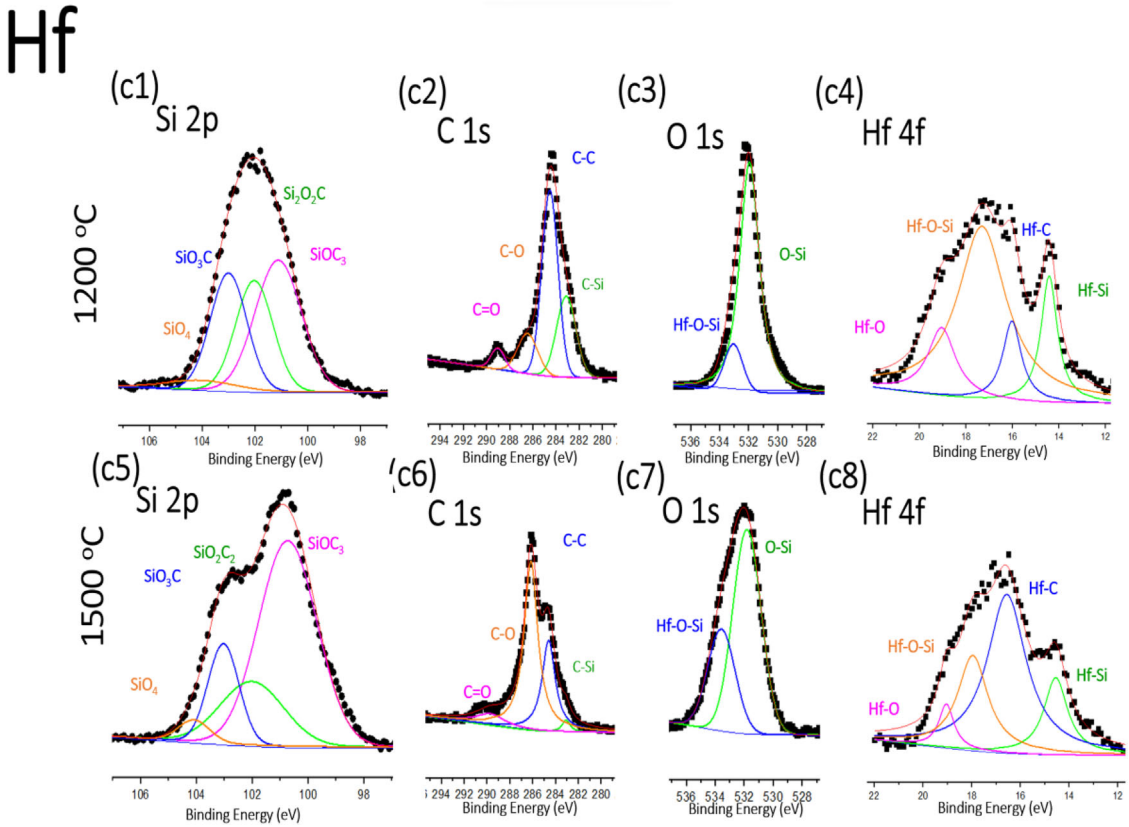


**FIGURE 4** Continued

in PDC structures, as suggested by the relative increase in $SiO_3C$ bonds with temperature in samples incorporating Ta fillers (see Figure 4).

C 1s convolutions permit identification of C—O (~286.5 eV) and C—C (~285 eV) and C—Si (~283 eV) bonds (see Figure 4). [64,66] In mixed bonding C is bonded to Si or to another C, hence, C—O bonds may correspond to oxygen termination in free carbon phases or adventitious carbons (e.g., absorbed $CO_2$). C—C and C—Si bonds may correspond to presence of free carbon and silicon carbide (SiC) domains, respectively. It should be noted that C—C and C—Si convolutions can be representative of mixed bonding domains as well.[5,19] C1s convolutions in Figure 4 indicate general increase in the amount of C—O (relative to C—C and C—Si) bonds with pyrolysis temperature, with exception of samples employing Ta fillers. This may indicate decrease in the relative amount of C—Si and C—C bonds in samples employing Nb, and Hf. Such a change may result from formation of more metal-Si bonds (e.g., metal silicates), loss of $SiO_xC_{4-x}$ mixed bonds (from phase separation), and/or carbothermal reduction of metal oxides by free carbon to form metal carbide at higher synthesis temperature, as suggested by Ta 4f, Nb 3d, and Hf 4f convolutions. The weak signal corresponding to metal bonds results from the low amount of the metal fillers in the compositions, as demonstrated below. Overall, the peak positions in metal convolutions are consistent with previous works and the current NIST database.[67–75] It is likely that C 1s convolutions do not show C-metal bonds due to their much lower relative amounts compared to C—C, C—Si, and C—O bonds.

Compositional analysis of the PDCs is done by survey-XPS experiments. This technique permits efficient elemental analysis of PDCs fine powders synthesized at high temperature (>1000°C), when residual hydrogen content is negligible.[33] The results from compositional analysis are summarized in Table 5. The compositions confirm presence of Si,C, O, and corresponding metals in all samples, it should be noted that the results further indicate that metals are present in minor amounts. This may in part be attributed to possible selection of metal-deficient portions of the crosslinked precursor for pyrolysis (*due to severe inhomogeneity of metal distribution*), as described in the crosslinking section. Typically, metal additives are introduced to preceramic polymers as compound precursors including metal oxides, metal tetrachlorides, and even organometallic acids (e.g., boric acid).[76–78] The Incorporation of metal powders, which are more reactive, may result in further loss of metal content from the formation of volatile metal complexes (e.g., ethoxides) at processing

**TABLE 5** Summary of $Si_aO_b(M)_cC_d$ compositions.

| Elemental composition by XPS | | | | | | | |
|---|---|---|---|---|---|---|---|
| | | Elements (at.%) | | | | | |
| Sample | Composition $Si_1O_a(M)_bC_c$ (normalized per Si) | C 1s | O 1s | Si 2p | Ta 4f | Nb 3d | Hf 4f |
| Ta-1200 | $Si_1O_{1.028}Ta_{0.012}C_{1.375}$ | 40.31 | 30.08 | 29.26 | .34 | – | – |
| Ta-1500 | $Si_1O_{1.009}Ta_{0.015}C_{1.342}$ | 39.87 | 29.97 | 29.7 | .45 | – | – |
| Nb-1200 | $Si_1O_{1.014}Nb_{0.006}C_{1.437}$ | 41.56 | 29.33 | 28.92 | – | .18 | – |
| Nb-1500 | $Si_1O_{0.725}Nb_{0.009}C_{1.136}$ | 39.58 | 25.25 | 34.83 | – | .32 | – |
| Hf-1200 | $Si_1O_{1.006}Hf_{0.018}C_{1.611}$ | 44.32 | 27.68 | 27.51 | – | – | .48 |
| Hf-1500 | $Si_1O_{0.855}Hf_{0.014.}C_{1.363}$ | 42.16 | 26.46 | 30.94 | – | – | .44 |

conditions.[79–81] Unreacted volatiles may continue to evolve during pyrolysis. As expected, the results suggest significant decrease in the O : Si (and O : M) as well as C : Si (and C: M) ratio with increasing pyrolysis temperature. This is consistent with carbothermal reduction of metal oxide and/or silica domains to form evolved CO and carbides of metal and/or silicon.[60–62]

Overall, incorporation of Ta metal appears to permit retention of greatest amount of O with increasing synthesis temperature. The C content is greatest in samples employing Hf metal fillers, in contrast O content is highest in specimens employing Ta. These differences are likely associated with dissimilarities in the relative amount of mixed bonds, metal carbide, and oxide phases in the microstructures, as suggested by HR-XPS spectra of the metal, including Ta 4f, Nb 3d, and Hf 4f convolutions.

## 3.1 | Thermodynamic stability and interdomain interactions

This investigation surveys the energy landscape for metal (Ta, Hf, Nb) incorporation in $Si_aO_b(M)_cC_d$. This permits identification of any differences in the stability trend resulting from choice of metal. Such fundamental understanding is essential for the development of a framework for stable incorporation of metal additives in PDC structures.

Thermodynamic analysis is done using thermochemical data obtained from calorimetry. Enthalpies of formation from elements ($\Delta H^\circ_{f,\,elem}$) and components ($\Delta H^\circ_{f,\,comp}$) is determined using enthalpies of dissolution ($\Delta H^\circ_{dis}$) and thermodynamic cycles. The free energy of formation depends on the change in enthalpy and entropy. Typically, the entropy term for formation from elements is negative, which results from confinement of gaseous $O_2$ in the structures, however, this is compensated by a highly exothermic enthalpy term. In contrast, the free energy of formation from crystalline components is dominated by enthalpy; the entropy term is of lower magnitude and may be positive because of possible disorder, which would further stabilize the structures. The results are summarized in Tables 6. Overall, the formation of all structures both from elements and from binary components is thermodynamically favorable.

An important consideration in the application of PDC structures is their propensity for oxidation. The oxidation enthalpies ($\Delta H^o_{Ox}$) correspond to change in enthalpy for oxidative decomposition of the PDCs into $SiO_2$, $CO_2$, and metal oxide at ambient conditions (see Tables 6). Overall, the enthalpic drive for oxidation increases in the following order: Hf-1500 < Nb-1500 < Ta-1500 < Hf-1200 < Ta-1200 < Nb-1200. This may indicate lower propensity for oxidation in specimens employing Hf fillers. In contrast, for samples synthesized at 1500°C Ta appears to be most energetically favorable for the oxidation reaction. Nb shows greatest enthalpic drive for oxidative decomposition in samples synthesized at 1200°C. Overall, choice of metal fillers appears to influence composition, microstructure, and enthalpic drive for oxidation in PDCs.

Since HR-XPS and XRD suggest presence of both metal carbide and metal oxide domains, enthalpies of formation from components are calculated relative to individual phase assemblages comprised of either metal oxide or metal carbide (see Tables 6). This permits identification of the most stable phase assemblage. Generally, the results in Tables 6 ($\Delta H^\circ_{f,\,comp}$) do not indicate significant difference from choice of either metal carbide or oxide as reference. The thermodynamic analysis further permits determination of effect of synthesis temperature on the stability of samples synthesized at 1200 and 1500°C. The more exothermic enthalpies of formation of samples pyrolyzed at 1500°C indicate more favorable enthalpic drive for microstructural modifications at higher synthesis temperature. The addition of Hf forms the most stable structures at all temperatures. Samples incorporating Nb (Nb-1200 and Nb-1500) display greatest thermodynamic stabilization with increasing pyrolysis temperatures (see

**TABLE 6** Summary of standard enthalpies of dissolution ($\Delta H_{dis}$), enthalpies of oxidation ($\Delta H^{o}_{Ox}$), enthalpies of formation from elements ($\Delta H^{\circ}_{f,\,elem}$), and enthalpies of formation from components ($\Delta H^{\circ}_{f,\,comp}$).

| Sample | Composition $Si_aO_bM_cC_d$ | $\Delta H_{dis}$ (kJ/mol) | $\Delta H^{o}_{Ox}$ (kJ/mol) | $\Delta H^{\circ}_{f,\,elem}$ (kJ/mol) | $\Delta H^{\circ}_{f,\,comp}$ (kJ/mol) |
|---|---|---|---|---|---|
| Nb-1200 | $Si_1O_{1.014}Nb_{0.006}C_{1.437}$ | −845.36 ± 6.62 | −900.67 ± 6.62 | −578.88 ± 6.94 | −82.80 ± 9.82 **(metal oxide)**<br>−81.40 ± 9.82 **(metal carbide)** |
| Ta-1200 | $Si_1O_{1.028}Ta_{0.012}C_{1.375}$ | −770.26 ± 6.48 | −825.01 ± 6.78 | −636.72 ± 7.10 | −137.82 ± 9.72 **(metal oxide)**<br>− 135.72 ± 9.72 **(metal carbide)** |
| Hf-1200 | $Si_1O_{1.006}Hf_{0.018}C_{1.611}$ | −749.49 ± 5.27 | −807.74 ± 5.64 | −754.70 ± 6.03 | −256.31 ± 8.97 **(metal oxide)**<br>−257.94 ± 8.97 **(metal carbide)** |
| Nb-1500 | $Si_1O_{0.725}Nb_{0.009}C_{1.136}$ | −715.87 ± 6.62 | −763.91 ± 6.62 | −600.05 ± 6.94 | −224.98 ± 9.60 **(metal oxide)**<br>−222.84 ± 9.60 **(metal carbide)** |
| Ta-1500 | $Si_1O_{1.009}Ta_{0.015}C_{1.342}$ | −721.20 ± 2.23 | −775.48 ± 2.99 | −676.34 ± 3.65 | −182.80 ± 7.85 **(metal oxide)**<br>−179.92 ± 7.85 **(metal carbide)** |
| Hf-1500 | $Si_1O_{0.855}Hf_{0.014.}C_{1.363}$ | −680.56 ± 5.57 | −733.64 ± 5.92 | −726.74 ± 6.29 | −292.54 ± 9.38 **(metal oxide)**<br>−293.43 ± 9.38 **(metal carbide)** |

$\Delta H^{\circ}_{f,\,comp}$ in Tables 6). In contrast specimens with Hf (Hf-1200 and Hf-1500) display the least stabilization difference between 1200 and 1500°C. Greater stability relative to crystalline components suggests more favorable interdomain interactions and/or more mixed bonding in the microstructures. The general trend of increase in stability with increasing synthesis temperature appears to be independent of choice of metal. It should be noted that overall, results from HR-XPS and XRD highlight consumption of metal-oxygen and formation of metal-carbon bonds between 1200–1500°C, perhaps implying a more stable incorporation of metal carbide fillers.

## 4 | CONCLUSIONS

This work investigates thermodynamic stabilization in $Si_aO_b(M)_cC_d$ structures incorporating Ta, Hf, or Nb. Generally, higher synthesis temperature promotes increase in the ratio of $SiOC_3$ : $SiO_3C$ mixed bonds. Ta metal fillers stabilize the formation of $SiO_3C$ bonds. Between 1200 and 1500°C higher synthesis temperature is consistent with greater thermodynamic stabilization of the structures. These results indicate most stable incorporation of Hf into SiOC microstructures, independent of synthesis temperature. Choice of metal filler impacts the microstructure and thermodynamic stability of the PDCs. Metal carbide fillers may form more stable $Si_aO_b(M)_cC_d$ structures. This work provides initial framework for the stable incorporation of metal fillers in PDCs.

## ACKNOWLEDGMENTS

Financial support from National Science Foundation (NSF) Partnerships for International Research and Education (PIRE) grant #1743701 is gratefully acknowledged.

## ORCID

*Alexandra Navrotsky* https://orcid.org/0000-0002-3260-0364

## REFERENCES

1. Colombo P, Mera G, Riedel R, Sorarù GD. Polymer-derived ceramics: 40 years of research and innovation in advanced ceramics. J Am Ceram Soc. 2010;93(7):1805–37.
2. Colombo P. Polymer derived ceramics: From nano-structure to applications. Lancaster, Pennsylvania: DEStech Publications, Inc; 2010.
3. Miele P, Bernard S, Cornu D, Toury B. Recent developments in polymer-derived ceramic fibers (PDCFs): preparation, properties and applications – a review. Soft Mater. 2007;4(2–4):249–86.
4. Duperrier S, Gervais C, Bernard S, Cornu D, Babonneau F, Balan C, et al. Design of a series of preceramic B-tri(methylamino)borazine-based polymers as fiber precursors: architecture, thermal behavior, and melt-spinnability. Macromolecules. 2007;40(4):1018–27.
5. Leonel GJ, Mujib SB, Singh G, Navrotsky A. Thermodynamic stabilization of crystalline silicon carbide polymer-derived ceramic fibers. Int J Ceram Eng Sci. 2022;4(5):315–26.
6. Luan X, Gu S, Zhang Q, Cheng L, Riedel R. An electrically conductive SiBCN film prepared via polymer-derived ceramic and chemical vapor deposition methods. Sens Actuators Phys. 2021;330:112824.
7. Goerke O, Feike E, Heine T, Trampert A, Schubert H. Ceramic coatings processed by spraying of siloxane precursors (polymer-spraying). J Eur Ceram Soc. 2004;24(7):2141–7.
8. Steyer TE. Shaping the future of ceramics for aerospace applications. Int J Appl Ceram Technol. 2013;10(3):389–94.
9. Saccone G, Gardi R, Alfano D, Ferrigno A, Del Vecchio A. Laboratory, on-ground and in-flight investigation of ultra high temperature ceramic composite materials. Aerosp Sci Technol. 2016;58:490–7.
10. Torrey JD, Bordia RK. Processing of polymer-derived ceramic composite coatings on steel. J Am Ceram Soc. 2008;91(1):41–5.

11. Soboyejo WO, Obayemi JD, Annan E, Ampaw EK, Daniels L, Rahbar N. Review of high temperature ceramics for aerospace applications. Adv Mater Res. 2016;1132:385–407.
12. Ngoumeni-Yappi R, Fasel C, Riedel R, Ischenko V, Pippel E, Woltersdorf J, et al. Tuning of the rheological properties and thermal behavior of boron-containing polysiloxanes. Chem Mater. 2008;20(11):3601–8.
13. Huang K, Elsayed H, Franchin G, Colombo P. 3D printing of polymer-derived SiOC with hierarchical and tunable porosity. Addit Manuf. 2020;36:101549.
14. Arai N, Faber KT. Hierarchical porous ceramics via two-stage freeze casting of preceramic polymers. Scr Mater. 2019;162:72–6.
15. Greil P. Near net shape manufacturing of polymer derived ceramics. J Eur Ceram Soc. 1998;18(13):1905–14.
16. Friedel T, Travitzky N, Niebling F, Scheffler M, Greil P. Fabrication of polymer derived ceramic parts by selective laser curing. J Eur Ceram Soc. 2005;25(2):193–7.
17. Jia Y, Ajayi TD, Morales J, Chowdhury MdAR, Sauti G, Chu S-H, et al. Thermal properties of polymer-derived ceramic reinforced with boron nitride nanotubes. J Am Ceram Soc. 2019;102(12):7584–93.
18. Ionescu E, Mera G, Riedel R. Polymer-derived ceramics (PDCs): materials design towards applications at ultrahigh-temperatures and in extreme environments. Nanotechnol Concepts Methodol Tools Appl. 2014;1:1108–39.
19. Mera G, Navrotsky A, Sen S, Kleebe H-J, Riedel R. Polymer - derived SiCN and SiOC ceramics – structure and energetics at the nanoscale. J Mater Chem A. 2013;1(12):3826–36.
20. Liu X, Li Y-L, Hou F. Fabrication of SiOC ceramic microparts and patterned structures from polysiloxanes via liquid cast and pyrolysis. J Am Ceram Soc. 2009;92(1):49–53.
21. Tressler RE. Recent developments in fibers and interphases for high temperature ceramic matrix composites. Compos Part Appl Sci Manuf. 1999;30(4):429–37.
22. Duan W, Yin X, Li Q, Liu X, Cheng L, Zhang L. Synthesis and microwave absorption properties of SiC nanowires reinforced SiOC ceramic. J Eur Ceram Soc. 2014;34(2):257–66.
23. Blum YD, MacQueen DB, Kleebe H-J. Synthesis and characterization of carbon-enriched silicon oxycarbides. J Eur Ceram Soc. 2005;25(2):143–9.
24. Barroso GS, Krenkel W, Motz G. Low thermal conductivity coating system for application up to 1000°C by simple PDC processing with active and passive fillers. J Eur Ceram Soc. 2015;35(12):3339–48.
25. Parcianello G, Bernardo E, Colombo P. Cordierite ceramics from silicone resins containing nano-sized oxide particle fillers. Ceram Int. 2013;39(8):8893–9.
26. Vakifahmetoglu C, Presser V, Yeon S-H, Colombo P, Gogotsi Y. Enhanced hydrogen and methane gas storage of silicon oxycarbide derived carbon. Microporous Mesoporous Mater. 2011;144(1):105–12.
27. Sarkar S, Gan Z, An L, Zhai L. Structural evolution of polymer-derived amorphous SiBCN ceramics at high temperature. J Phys Chem C. 2011;115(50):24993–5000.
28. Zhou S, Mei H, Chang P, Lu M, Cheng L. Molecule editable 3D printed polymer-derived ceramics. Coord Chem Rev. 2020;422:213486.
29. Scheffler M, Greil P, Berger A, Pippel E, Woltersdorf J. Nickel-catalyzed in situ formation of carbon nanotubes and turbostratic carbon in polymer-derived ceramics. Mater Chem Phys. 2004;84(1):131–9.
30. Greil P. Polymer derived engineering ceramics. Adv Eng Mater. 2000;2(6):339–48.
31. Wang X, Wang J, Wang H. Performance and structural evolution of high-temperature organic adhesive for joining Al2O3 ceramics. Int J Adhes Adhes. 2013;45:1–6.
32. Hernández-Rodríguez P, López-Honorato E. Polymer derived SiC environmental barrier coatings with superwetting properties. Ceram Int. 2017;43(14):11289–95.
33. Leonel GJ, Guo X, Singh G, Navrotsky A. Compositional analysis of SiOC(H) powders: a comparison of X-ray photoelectron spectroscopy (XPS) and combustion analysis. Ceramics. 2023;6(1):74–85.
34. Morcos RM, Navrotsky A, Varga T, Blum Y, Ahn D, Poli F, et al. Energetics of SixOyCz polymer-derived ceramics prepared under varying conditions. J Am Ceram Soc. 2008;91(9):2969–74.
35. Varga T, Navrotsky A, Moats JL, Morcos RM, Poli F, Müller K, et al. Thermodynamically stable SixOyCz polymer-like amorphous ceramics. J Am Ceram Soc. 2007;90(10):3213–9.
36. Niu M, Gao H, Zhao Z, Wang H, Su L, Zhuang L, et al. Radiation effects in the crystalline–amorphous SiOC polymer-derived ceramics: insights from experiments and molecular dynamics simulation. ACS Appl Mater Interfaces. 2021;13(33):40106–17.
37. Sugie C, Navrotsky A, Lauterbach S, Kleebe H-J, Mera G. Structure and thermodynamics of silicon oxycarbide polymer-derived ceramics with and without mixed-bonding. Materials. 2021;14(15):4075.
38. Zlotnik S, Sahu SK, Navrotsky A, Vilarinho PM. Pyrochlore and perovskite potassium tantalate: enthalpies of formation and phase transformation. Chem – Eur J. 2015;21(13):5231–7.
39. Navrotsky A. Progress and new directions in calorimetry: a 2014 Perspective. J Am Ceram Soc. 2014;97(11):3349–59.
40. Allison TC. NIST-JANAF thermochemical tables - SRD 13. 2013.
41. Kornilov AN, Ushakova IM, Huber EJ, Holley CE. The enthalpy of formation of hafnium dioxide. J Chem Thermodyn. 1975;7(1):21–6.
42. Mah AD. Heats of formation of zirconium carbide and hafnium carbide. U.S. Department of the Interior, 1849 C Street NW, Washington, DC: Bureau of Mines; 1964.
43. Ikezawa Y, Sawatari T, Terashima H. In situ FTIR study of pyridine adsorbed on Au(111), Au(100) and Au(110) electrodes. Electrochimica Acta. 2001;46(9):1333–7.
44. Yelil Arasi A, Juliet Latha Jeyakumari J, Sundaresan B, Dhanalakshmi V, Anbarasan R. The structural properties of poly(aniline)—analysis via FTIR spectroscopy. Spectrochim Acta A Mol Biomol Spectrosc. 2009;74(5):1229–34.
45. Benning LG, Phoenix VR, Yee N, Tobin MJ. Molecular characterization of cyanobacterial silicification using synchrotron infrared micro-spectroscopy1 1Associate editor: J. P. Amend. Geochim Cosmochim Acta. 2004;68(4):729–41.
46. Osswald J, Fehr KT. FTIR spectroscopic study on liquid silica solutions and nanoscale particle size determination. J Mater Sci. 2006;41(5):1335–9.
47. Lubguban J, Rajagopalan T, Mehta N, Lahlouh B, Simon SL, Gangopadhyay S. Low-k organosilicate films prepared by tetravinyltetramethylcyclotetrasiloxane. J Appl Phys. 2002;92(2):1033–8.

48. Mastalerz M, Marc Bustin R. Electron microprobe and micro-FTIR analyses applied to maceral chemistry. Int J Coal Geol. 1993;24(1):333–45.
49. Thomas PS, Guerbois J-P, Russell GF, Briscoe BJ. FTIR Study of the thermal degradation of poly(vinyl Alcohol). J Therm Anal Calorim. 2001;64(2):501–8.
50. Chen Y, Caro LD, Mastalerz M, Schimmelmann A, Blandón A. Mapping the chemistry of resinite, funginite and associated vitrinite in coal with micro-FTIR. J Microsc. 2013;249(1): 69–81.
51. Mendelovici E, Frost RL, Kloprogge JT. Modification of chrysotile surface by organosilanes: an IR–photoacoustic spectroscopy study. J Colloid Interface Sci. 2001;238(2):273–8.
52. Canaria CA, Lees IN, Wun AW, Miskelly GM, Sailor MJ. Characterization of the carbon–silicon stretch in methylated porous silicon—observation of an anomalous isotope shift in the FTIR spectrum. Inorg Chem Commun. 2002;5(8): 560–4.
53. Wu XC, Cai RQ, Yan PX, Liu WM, Tian J. SiCN thin film prepared at room temperature by r.f. reactive sputtering. Appl Surf Sci. 2002;185(3):262–6.
54. Castro DC, Cavalcante RP, Jorge J, Martines MAU, Oliveira LCS, Casagrande GA, et al. Synthesis and characterization of mesoporous $Nb_2O_5$ and its application for photocatalytic degradation of the herbicide methylviologen. J Braz Chem Soc. 2015:27. https://doi.org/10.5935/0103-5053.20150244
55. Ramadoss A, Krishnamoorthy K, Kim SJ. Novel synthesis of hafnium oxide nanoparticles by precipitation method and its characterization. Mater Res Bull. 2012;47(9):2680–4.
56. Zhang N, Li L, Li G. Nanosized amorphous tantalum oxide: a highly efficient photocatalyst for hydrogen evolution. Res Chem Intermed. 2017;43(9):5011–24.
57. Din Babar ZUd, Fatheema J, Arif N, Anwar MS, Gul S, Iqbal M, et al. Magnetic phase transition from paramagnetic in Nb 2 AlC-MAX to superconductivity-like diamagnetic in Nb 2 C-MXene: an experimental and computational analysis. RSC Adv. 2020;10(43):25669–78.
58. Jafari B, Rezaei E, Dianat MJ, Abbasi M, Hashemifard SA, Khosravi A, et al. Development of a new composite ceramic membrane from mullite, silicon carbide and activated carbon for treating greywater. Ceram Int. 2021;47(24):34667–75.
59. Alper JP, Kim MS, Vincent M, Hsia B, Radmilovic V, Carraro C, et al. Silicon carbide nanowires as highly robust electrodes for micro-supercapacitors. J Power Sources. 2013;230: 298–302.
60. Kwon H, Kim W, Kim J. Stability domains of NbC and Nb(CN) during carbothermal reduction of niobium oxide. J Am Ceram Soc. 2015;98(1):315–9.
61. Sacks MD, Wang C-A, Yang Z, Jain A. Carbothermal reduction synthesis of nanocrystalline zirconium carbide and hafnium carbide powders using solution-derived precursors. J Mater Sci. 2004;39(19):6057–66.
62. Réjasse F, Trolliard G, Rapaud O, Maître A, David J. TEM study of the reaction mechanisms involved in the carbothermal reduction of hafnia. RSC Adv. 2015;5(56):45341–50.
63. Paprocki K, Dittmar-Wituski A, Trzciński M, Szybowicz M, Fabisiak K, Dychalska A. The comparative studies of HF CVD diamond films by Raman and XPS spectroscopies. Opt Mater. 2019;95:109251.
64. Sang Z, Zhao Z, Su D, Miao P, Zhang F, Ji H, et al. SiOC nanolayer wrapped 3D interconnected graphene sponge as a high-performance anode for lithium ion batteries. J Mater Chem A. 2018;6(19):9064–73.
65. Zhang X, Wang D, Qiu X, Ma Y, Kong D, Müllen K, et al. Stable high-capacity and high-rate silicon-based lithium battery anodes upon two-dimensional covalent encapsulation. Nat Commun. 2020;11(1):3826.
66. Greczynski G, Hultman L. C 1s Peak of adventitious carbon aligns to the vacuum level: dire consequences for material's bonding assignment by photoelectron spectroscopy. ChemPhysChem. 2017;18(12):1507–12.
67. Lahoz R, Espinós JP, Yubero F, González-Elipe AR, Fuente de la GF. "In situ" XPS studies of laser-induced surface nitridation and oxidation of tantalum. J Mater Res. 2015;30(19): 2967–76.
68. Powell C. NIST X-ray photoelectron spectroscopy database. Gaithersburg MD: National Institute Of Standards And Technology; 1989.
69. Lee S, Yun D-J, Rhee S-W, Yong K. Atomic layer deposition of hafnium silicate film for high mobility pentacene thin film transistor applications. J Mater Chem. 2009;19(37):6857–64.
70. Hans K, Latha S, Bera P, Barshilia HC. Hafnium carbide based solar absorber coatings with high spectral selectivity. Sol Energy Mater Sol Cells. 2018;185:1–7.
71. Gupta A, Mittal M, Singh MK, Suib SL, Pandey OP. Low temperature synthesis of NbC/C nano-composites as visible light photoactive catalyst. Sci Rep. 2018;8(1):13597.
72. Chang Y-Y, Huang H-L, Chen Y-C, Hsu J-T, Shieh T-M, Tsai M-T. Biological characteristics of the MG-63 human osteosarcoma cells on composite tantalum carbide/amorphous carbon Films. PLOS One. 2014;9(4):e95590.
73. Hellwig M, Milanov A, Barreca D, Deborde J-L, Thomas R, Winter M, et al. Stabilization of amide-based complexes of niobium and tantalum using malonates as chelating ligands: precursor chemistry and thin film deposition. Chem Mater. 2007;19(25):6077–87.
74. Mullapudi GSR, Velazquez-Nevarez GA, Avila-Avendano C, Torres-Ochoa JA, Quevedo-López MA, Ramírez-Bon R. Low-temperature deposition of inorganic–organic HfO2–PMMA hybrid gate dielectric layers for high-mobility ZnO thin-film transistors. ACS Appl Electron Mater. 2019;1(6): 1003–11.
75. Aubry D, Volcke C, Arnould Ch, Humbert C, Thiry PA, Delhalle J, et al. Molecular functionalization of tantalum oxide surface towards development of apatite growth. Appl Surf Sci. 2009;255(9):4765–72.
76. Lyu Y, Tang H, Zhao G. Effect of Hf and B incorporation on the SiOC precursor architecture and high-temperature oxidation behavior of SiHfBOC ceramics. J Eur Ceram Soc. 2020;40(2):324–32.
77. Abass MA, Syed AA, Gervais C, Singh G. Synthesis and electrochemical performance of a polymer-derived silicon oxycarbide/boron nitride nanotube composite. RSC Adv. 2017;7(35):21576–84.
78. Ionescu E, Linck C, Fasel C, Müller M, Kleebe H, Riedel R. Polymer-derived SiOC/ZrO2 ceramic nanocomposites with excellent high-temperature stability. J Am Ceram Soc. 2010;93(1):241–50.

79. Okamura H, Bowen HK. Preparation of alkoxides for the synthesis of ceramics. Ceram Int. 1986;12(3):161–71.
80. Yang S, Chen Y, Yang H, Liu Y, Tang M, Qiu G. Preparation of high-purity tantalum ethoxide by vacuum distillation. Trans Nonferrous Met Soc China. 2008;18(1):196–201.
81. Bickmore CR, Waldner KF, Treadwell DR, Laine RM. Ultrafine spinel powders by flame spray pyrolysis of a magnesium aluminum double alkoxide. J Am Ceram Soc. 1996;79(5):1419–23.

**How to cite this article:** Leonel GJ, Scharrer M, Singh G, Navrotsky A. Structural and thermodynamic analysis of metal filler incorporations in $Si_aO_b(M)_cC_d$ polymer derived ceramics: Ta, Hf, Nb. Int J Appl Ceram Technol. 2023;20:3395–3406. https://doi.org/10.1111/ijac.14476